Nanoscale

PAPER

View Article Online
View Journal

Cite this: DOI: 10.1039/c6nr01206j

Zirconium–metalloporphyrin frameworks as a three-in-one platform possessing oxygen nanocage, electron media, and bonding site for electrochemiluminescence protein kinase activity assay†

Guang-Yao Zhang,[a] Chang Cai,[a] Serge Cosnier,[b] Hai-Bo Zeng,[c] Xue-Ji Zhang[a] and Dan Shan*[a]

A Zr-based metal–organic framework with zinc tetrakis(carboxyphenyl)-porphyrin (ZnTCPP) groups (MOF-525-Zn) was utilized to develop a novel electrochemiluminescence (ECL) biosensor for highly sensitive protein kinase activity assay. In this work, in terms of ECL measurements and cyclic voltammetry, the cathodic ECL behaviors of MOF-525-Zn in aqueous media were thoroughly investigated for the first time. The photoelectric active groups ZnTCPP on the MOF-525-Zn frameworks could promote the generation of singlet oxygen ($^1O_2$) *via* a series of electrochemical and chemical reactions, resulting in a strong and stable red irradiation at 634 nm. Additionally, the surfactant tetraoctylammonium bromide (TOAB) further facilitated dissolved oxygen to interact with the active sites ZnTCPP of MOF-525-Zn. Furthermore, the inorganic Zr–O clusters of MOF-525-Zn were simultaneously served as the recognition sites of phosphate groups. And then, an ultrasensitive ECL sensor was proposed for protein kinase A (PKA) activity detection with a linear range from 0.01 to 20 U mL^{-1} and a sensitive detection limit of 0.005 U mL^{-1}. This biosensor can also be applied for quantitative kinase inhibitor screening. Finally, it exhibits good performance with high stability and acceptable fabrication reproducibility, which provide a valuable strategy for clinic diagnostics and therapeutics.

Received 11th February 2016,
Accepted 16th May 2016

DOI: 10.1039/c6nr01206j

www.rsc.org/nanoscale

Introduction

Protein phosphorylation catalyzed by protein kinases plays a vital role in the regulation of cellular functions involving metabolism, cell growth, gene transcription and survival differentiation.[1–3] The overexpression of protein kinases leads to abnormal protein phosphorylation states, which is highly relevant to a series of diseases including cancers and Alzheimer's diseases.[4–6] Protein kinases have been regarded as important biomarkers for diseases diagnostic and constitute targets for evaluation of therapeutic efficacy by using the potential inhibitors of kinases. Therefore, accurate identification of protein kinase activity and kinase inhibitors screening are greatly significant and necessary for further understanding the molecular mechanism of signal transduction, clinical diagnosis and molecular-targeted therapy.

Up till now, the electrochemical method has established itself as a powerful tool for ultrasensitive protein kinase activity detection. In comparison with several other techniques such as fluorescence,[7] colorimetric sensing,[8] Raman spectroscopy,[9] and mass spectrometry,[10] an electrochemical approach has captured considerable attention on account of its high sensitivity, portability, simplicity, and low cost. In particular, electrochemiluminescence (ECL), an electrogenerated chemiluminescence technique, takes synergized advantages of both electrochemistry and chemiluminescence, resulting in low background noise and intrinsic high sensitivity for analysis.[11] Especially, the enhanced ECL analysis strategy based on metal nanoparticles or quantum dots (QDs) is more attractive for PKA biosensor.[12–14] Though some good experimental results including high sensitivity, low detection limit and wide

[a]*Sino-French Laboratory of Biomaterials and Bioanalytical Chemistry, School of Environmental and Biological Engineering, Nanjing University of Science and Technology, Nanjing 210094, China. E-mail: danshan@njust.edu.cn, danshan@yzu.edu.cn; Fax: +86-025-84303107; Tel: +86-025-84303107*
[b]*Univ. Grenoble Alpes, Département de Chimie Moléculaire, UMR CNRS 5250, 570 rue de la Chimie, CS 40700, 38058 Grenoble cedex 9, France*
[c]*Institute of Optoelectronics & Nanomaterials, Jiangsu Key Laboratory of Advanced Micro & Nano Materials and Technology, College of Material Science and Engineering, Nanjing University of Science and Technology, Nanjing 210094, China*
†Electronic supplementary information (ESI) available. See DOI: 10.1039/c6nr01206j

linear range were obtained by using these ECL methods, the primary ECL methodologies depend on the introduction of exogenous coreactant such as H_2O_2 and $Na_2S_2O_3$, which may be damage to biological molecules. Moreover, these ECL methods are easily affected by the complex biological environment,[15] thereby affecting the stability and reproducibility of PKA assay. In view of these, it is imperative to explore green and efficient luminophores for the development of ECL bioassay.

ECL behaviours involving oxygen molecules have been previously reported. Allen J. Bard's group proposed a mechanism for producing singlet oxygen ($^1O_2$) by the ECL electron-transfer annihilation reaction with sufficient energy in nonaqueous media, such as superoxide ion ($O_2^{\bullet-}$) and ferricenium cation,[16] $O_2^{\bullet-}$ and Tri-*n*-propylamine cation ($TPrAH^{\bullet+}$).[17] Porphyrin compounds as visible-light photosensitizers, generate $^1O_2$ efficiently, and are already applied in clinics in photodynamic therapy (PDT).[18,19] In addition, metalloporphyrins are essential to ubiquitous biological functionalities of mammalian life, for example oxygen transport and storage.[20] Recently, our laboratory demonstrated the cathodic ECL mechanism of $^1O_2$ induced by the electroactive zinc porphyrin in aqueous media: the intermediate anion of zinc porphyrin ($Zn^{\bullet+}$) *via* successive electrochemical reduction could oxidize $O_2^{\bullet-}$ to $^1O_2$,[21] and realized the highly sensitive detection of zinc finger protein.[22]

Metal–organic frameworks (MOFs), also known as coordination polymers (CPs), are a class of porous materials constructed from metal-containing nodes and organic linkers.[23] Owing to high specific surface areas, well-ordered porous structures and structural tunability,[24,25] MOFs have achieved a wide range of applications including gas storage,[26] biomedicine,[27] catalysis,[28] sensing,[29,30] and separation.[31] The applications of MOFs in the field of electrochemistry, used as electrode materials or electrocatalysts, have also attracted wide attention,[32] especially oxygen reduction reaction (ORR), a fundamental reaction in energy converting systems such as fuel cells.[33,34] Actually, as an ORR electrocatalyst,[35,36] MOF can play an important role as an oxygen container and facilitate some interactions between the surface of the pores and the oxygen molecules simultaneously.[37,38] Among various MOFs, metal–metalloporphyrin frameworks (MMPFs), constructed from porphyrinic or metalloporphyrinic ligands, have attracted intensive research interest because of the remarkable properties of porphyrin molecules, such as biochemical, enzymatic, and photochemical functions.[39] Associated with the ECL properties of zinc porphyrin inducing $^1O_2$ previously discussed, zinc porphyrin-based MOFs also possess similar ECL properties.

On the other hand, it has been well documented that some Zr-based materials including zirconium oxide (ZrO_2), magnetic zirconium hexacyanoferrate(II) nanoparticles (ZrHCF MNPs) and Zr-based MOFs, have been successfully applied to the selective enrichment of phosphopeptides and the assembled immobilization of DNA probe with the aid of the coordination binding zirconium to phosphate groups of biomolecules.[40–44] Besides, on the basis of "soft and hard acids and bases" theory, Zr(IV) cation and carboxylate anion pertain to hard acid and hard base, respectively, which makes the coordination bonds between zirconium and carboxylic oxygen very strong and potentially tolerant against attack from water, acid, and even base. For this, some Zr-carboxylate MOFs possess excellent stability in aqueous media,[45–47] which is of great value to biological analysis.

With all these in mind, for the first time, we have employed a very stable microporous zirconium–(zinc)porphyrin MOF, MOF-525-Zn as a three-in-one platform possessing oxygen nanocage, electron media, and bonding site in an ECL biological analysis system in presence of O_2. The ECL property of $^1O_2$ induced by the electroactive zinc tetrakis(carboxyphenyl)-porphyrin (ZnTCPP) in the presence of the amphiphilic tetraoctylammonium bromide (TOAB) in aqueous media, was used for highly sensitive protein kinase activity assay and inhibitor screening, while Zr–O clusters of MOF-525-Zn acted as anchorages for phosphate groups. Herein, the ZnTCPP linkers in MOF-525-Zn behaved as ECL active centers depended on the enrichment of oxygen molecules from the high porosity and tunable structures of MOFs, and the amphiphilic membrane TOAB could facilitate dissolved oxygen around the electro-catalytic ZnTCPP molecules. We unveiled the underlying ECL mechanism of generating $^1O_2$ based on the electroactive ZnTCPP of MOF-525-Zn with TOAB in aqueous media. Furthermore, as shown in Scheme 1, MOF-525-Zn could be firmly assembled on phosphorylated kemptide modified electrode on the basis of the high affinity of Zr–O clusters toward phosphate groups, followed by the activation of TOAB film. In the oxygen-enriched aqueous buffer, the fabricated electrode could be applied for the highly sensitive ECL protein kinase A (PKA) activity detection. Meanwhile, the PKA activities evaluation in complex biological samples and kinase inhibitor screening were also conducted. It is envisioned that the MOF-525-Zn and similar porphyrinic MOFs would have potential applications in ultrasensitive chemical sensing and even in accurately clinic diagnostic and drug discovery.

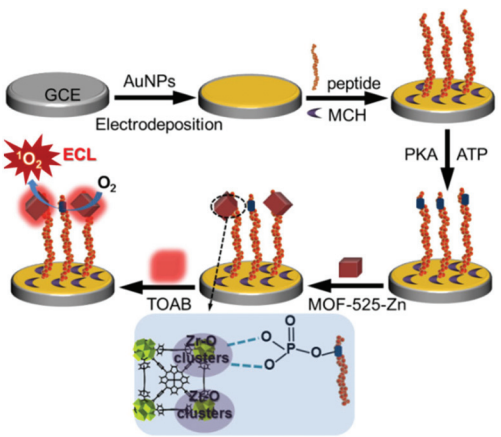

Scheme 1 Schematic representation of the MOF-525-Zn-based ECL biosensor for PKA assay.

Experimental section

Materials and reagents

Zirconium(IV) chloride, benzoic acid, *N*,*N*-dimethylformamide (DMF), 6-mercapto-1-hexanol (MCH, 97%), Tris(2-carboxyethyl) phosphine hydrochloride (TCEP), protein kinase A (PKA; catalytic subunit from bovine heart), ellagic acid, *N*-(3-chlorophenyl)-6,7-dimethoxy-4-quinazolinamine (Tyrphostin AG1478), adenosin triphosphate (ATP), tetraoctylammonium bromide (TOAB), Tris(hydroxymethyl) aminomethane (Tris) and *N*-(2-hydroxyethyl)piperazine-*N*′-(2-ethanesulfonic acid) (HEPES) sodium salt were purchased from Sigma-Aldrich Chemical Co., Ltd (Shanghai, China). Cysteine-kemptide (CLRRASLG) was obtained from GL Biochem (Shanghai, China). Chloroauricacid trihydrate ($HAuCl_4{\cdot}3H_2O$), zinc(II) *meso*-tetra(4-carboxyphenyl) porphine (ZnTCPP) and *meso*-tetra (4-carboxyphenyl)porphyrin (TCPP) were procured from J&K Chemical Ltd (Shanghai, China). Potassium ferricyanide [$K_3Fe(CN)_6$] and potassium ferrocyanide [$K_4Fe(CN)_6$] was purchased from Sinopharm Chemical Reagent Co., Ltd (Beijing, China). All other reagents were of analytical grade and were used without further purification. Ultrapure water obtained from a Millipore water purification system (≥18 MΩ, Milli-Q, Millipore) was used in all measurements. Human serum samples were provided by Jiangsu Province Tumor Hospital.

Apparatus

The morphology was investigated with a XL-30E scanning electron microscope (SEM). Fourier-transformation infrared (FT-IR) spectra were obtained with an IR-Prestige-21 FT-IR spectrometer (Shimadzu Co., Japan). Powder X-ray diffraction patterns (PXRD) were recorded on a Bruker D8-Focus Bragg-Brentano X-ray Powder diffractometer equipped with a Cu sealed tube (λ = 1.54178 Å) at room temperature. N_2 adsorption–desorption isotherms were measured using a Micrometritics ASAP 2020 system at 77 K. The water contact angle (CA) measurements were performed by the sessile drop technique using an Optical Tensionmeter (Theta Lite, Finland) under ambient laboratory conditions. A drop of distilled water was applied to the surface of modified glass plates, and the CA measurements were carried out within 30 s of the contact. A CHI 660D electrochemical workstation (CHI Co., USA) was used for cyclic voltammetry (CV) measurements. Electrochemical impedance spectroscopy (EIS) measurements were carried out using an Autolab PGSTAT30 (Eco chemie, The Netherlands) controlled by NOVA 1.10 software. The EIS measurements were performed in 0.1 M KCl containing 5 mM $[Fe(CN)_6]^{3-/4-}$. The amplitude of the applied sine wave potential was 5 mV. The impedance measurements were recorded at a bias potential of 290 mV within the frequency range of 0.1 Hz to 10 kHz. ECL measurements were carried out on an MPI-E multifunctional electrochemical and chemiluminescent analytical system (Xi'an Remex Analytical Instrument Co., Ltd, China) in which the emission window lays above the photomultiplier tube biased at −800 V. Steady-state photoluminescence (PL) spectra and the ECL spectra were recorded by an Edinburgh FLS920 fluorescence spectrometer (Livingston, UK). All electrochemical studies were performed with a conventional three electrode system. An Ag/AgCl electrode and a Pt wire electrode were used as reference and counter electrodes, respectively. A modified glassy carbon (GCE, 5 mm in diameter) was used as working electrodes.

Synthesis of MOF-525 and MOF-525-Zn

The MOFs were synthesized by a solvothermal process based on the previous report with minor modifications.[48,49] Typically, $ZrCl_4$ (75 mg), TCPP (30 mg), and benzoic acid (1750 mg) in 10 mL of DMF were ultrasonically dissolved in a 20 mL Pyrex vial. The mixture was heated to 120 °C in an oven for 48 h. After cooling down to room temperature, dark red crystals were harvested by centrifugation, named as MOF-525. MOF-525 with ZnTCPP was similarly synthesized, named as MOF-525-Zn.

Fabrication of PKA assay

The procedure for the preparation of PKA assay is illustrated in Scheme 1. The GCE was polished carefully with 0.3 and 0.05 μm of α-Al_2O_3 powder and sonicated sequentially in ethanol and double-distilled water. Prior to immobilization of kemptide, the pretreated electrode was immersed in $HAuCl_4$ solution for the electrodeposition of a nanogold layer at a potential of −0.2 V for 60 s. After being cleaned with water and dried with N_2, the gold nanoparticles-modified GCE was incubated with 20 μL of 200 μM cysteine terminated kemptide (dissolved in 10 mM Tris-HCl containing 10 mM TCEP, pH 7.4) at room temperature for 12 h. After being washed thoroughly with buffer solution, the electrode was immersed into 1.0 mM MCH for 1 h to block the unspecific sites and then washed thoroughly with blank PBS. PKA-catalyzed peptide phosphorylation was performed by incubating the modified electrode into an assay buffer solution (20 mM Tris-HCl and 20 mM $MgCl_2$, pH 7.4) containing different concentrations of PKA and ATP at 37 °C for 1 h. After rinsing, the obtained phosphorylated peptides modified electrode is further incubated with 1 mg mL^{-1} MOF-525-Zn at 37 °C for 1 h. After rinsing thoroughly with double-distilled water, 10 μL of 10 mM TOAB was spread on the surface of the modified electrode and dried at ambient temperature. Finally, the electrode would generate ECL signal in the O_2-saturated aqueous electrolyte solution and gave the quantitative criteria for the proposed PKA assay. For inhibiting the activity of PKA, the procedures were similar as above, except for a desired concentrations of inhibitor were added in the PKA assay buffer solutions.

Results and discussion

Characterization of the MOF-525 and MOF-525-Zn

MOF-525 consists of $Zr_6O_4(OH)_4$ clusters units linked by either porphyrin ligand, as shown in Scheme 2A. Different from the 12-connected Zr_6 cluster observed in the UiO-66 and 8-con-

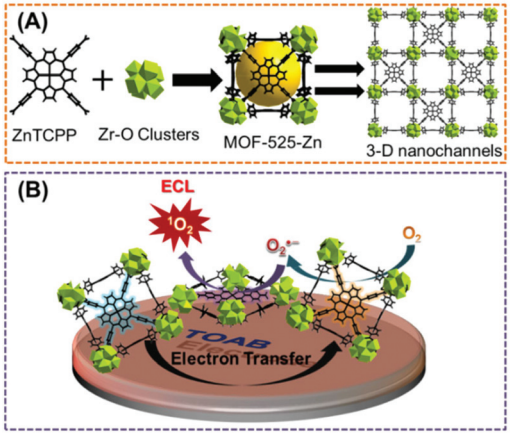

Scheme 2 Schematic illustration for the construction of MOF-525-Zn (A) and the ECL mechanism of singlet oxygen based on GCE/MOF-525-Zn/TOAB (B).

nected Zr_6 in MOF-525, only six edges of the $Zr_6O_4(OH)_4$ clusters are bridged by carboxylates from TCPP (or ZnTCPP) ligands in MOF-525. With the reduced number of carboxylate linkers, the new $Zr_6O_4(OH)_4$ cluster allows more free space, which eventually leads to the formation of three-dimensional (3-D) nanochannels.

The morphologies of the as-synthesized MOF-525 and MOF-525-Zn were characterized by SEM. As shown in Fig. 1A, the crystals of the MOF-525-Zn are uniform and exist as cubic morphology with the size range from 3 to 6 μm, which exists no significant differences from the MOF-525 (inset of Fig. 1A),

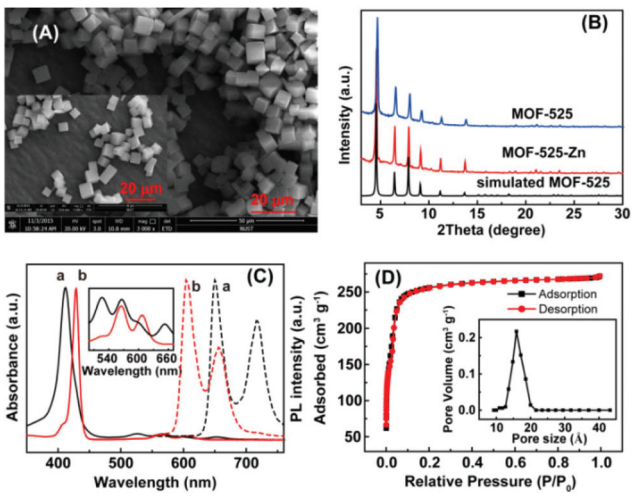

Fig. 1 (A) SEM image of MOF-525-Zn. Inset A: MOF-525. (B) Powder XRD patterns for simulated and experimental MOF-525 samples. (C) UV-visible and PL emission (λ_{ex} = 430 nm) spectra of (a) MOF-525 and (b) MOF-525-Zn in 1.0 M NaOH aqueous solutions. Inset: enlarged spectra in the Q-band region. (D) The nitrogen adsorption–desorption isotherm of MOF-525-Zn at 77 K, 1 atm. Inset D: the DFT pore size distribution of MOF-525-Zn.

suggesting that the growth process of MOF-525 crystals is not relevant to the metalation of porphyrin ligand.

The powder X-ray diffraction (PXRD) pattern of the MOF-525 powder was displayed in Fig. 1B. Diffraction peaks at 4.5°, 6.4°, 7.8°, 9.1°, 11.2° and 13.7° can be observed in the pattern of the MOF-525 powder, all of these peaks match with the simulated XRD pattern of MOF-525 reported previously.[50]

The UV-visible and PL emission spectra of the MOF-525 and MOF-525-Zn digested in 1.0 M NaOH aqueous solutions were shown in Fig. 1C. The UV-visible spectrum of MOF-525 (curve a, solid) showed a Soret band at 412 nm tailing with four Q bands located at 526, 566, 600, and 653 nm (inset of Fig. 1C, solid). This spectrum agrees well with the UV-visible spectrum of free-based TCPP reported previously.[51] For the MOF-525-Zn (curve b, solid), a typical Soret band at 429 nm and three Q bands located at 523, 565 and 607 nm can be clearly observed (inset of Fig. 1C, solid); this result is consistent with the UV-visible spectrum of ZnTCPP previously reported by Elena Galoppini *et al.*,[52] confirming that the successful encapsulation of porphyrin units in the frameworks. Moreover, in comparison to the MOF-525, the Soret peak of MOF-525-Zn was red shifted by 17 nm, which was construed as no apparent J-aggregates in addition to the abatement of π-conjugation.[53] From this, the optimal PL exciting wavelength $(\lambda_{ex})_{opt}$, further deflected the static PL properties of MOF-525 and MOF-525-Zn (Fig. 1C, dashed). As for MOF-525, one strong peak at 650 nm and a lesser at 716 nm were observed (curve a, dashed), in comparison, which decreased to the major at 604 nm for MOF-525-Zn along with a shoulder at 656 nm (curve b, dashed). It indicated that the zinc coordination affected on both ground and excited states of porphyrin. An internal conversion from Soret to Q-band must occur after the excitation as the emission maxima partially coincided with Q bands.[53] Association to the fundamentals of photodynamic therapy based on porphyrin, this PL survey can give us some inspiration on the ECL properties of porphyrin-based materials and oxygen molecules.

In addition, organo-functional groups in the MOF-525-Zn was further compared with ZnTCPP by FT-IR spectra (Fig. S1†), the positions of the peaks were generally consistent with ZnTCPP, supporting the conclusion that all the ZnTCPP units in the MOF-525-Zn were assembled successfully.

The N_2 adsorption–desorption isotherms of the MOF-525-Zn were also measured, as displayed in Fig. 1D, it shows a typical type-I isotherm, which is consistent with the crystal structure. Surface area analysis of MOF-525-Zn by the Brunauer–Emmett–Teller (BET) method gave surface areas of 2126 $m^2\ g^{-1}$. The experimental total pore volume was as high as 1.15 $cm^3\ g^{-1}$. In addition, the pore size distribution of the MOF-525-Zn was estimated by the density functional theory (DFT) simulation (inset of Fig. 1D), demonstrating a pore size of 1.7 nm, which is in excellent agreement with the value previously reported by Ho *et al.*[48,49] Such highly regular porous structure and high density of 3-D open channels enable this material with high gas storage capacity and are helpful for the enrichment of reaction substrates. Similarly, the adsorption of

oxygen molecules by microporous materials typically derived from some interactions between the surface of the pores and oxygen molecules, and from the fact that they are in an unusual state originating from an electronic effect and a confinement effect.[37] Based on metalloporphyrins as a catalyst in many redox-active reactions involving molecular oxygen,[54] porphyrinic MOFs are particularly well-suited for this challenge over other solid-state materials because of the high surface and intrinsic open structure.[55] Hence, the exposure of active sites to molecular oxygen in the 3D nanocage will promote further reduction of oxygen.

Electrochemical and ECL investigations

Since it is well known that Zr-based porphyrinic MOFs possess the wide-pH-range stability in the aqueous solutions and the dye characteristic of involved porphyrin center,[45] the MOF-525 and MOF-525-Zn are expected to be suitable for electrochemical applications in aqueous media. Electrochemical and ECL properties of MOF-525 and MOF-525-Zn were investigated on the GCE in aqueous media. In this experiment, 10 μL of 10 mM TOAB was spread on the surface of GCE, MOF-525 and MOF-525-Zn modified GCE, and dried at ambient temperature, named as GCE/TOAB, GCE/MOF-525/TOAB and GCE/MOF-525-Zn/TOAB. Fig. 2A and B shows a typical CV and ECL response of different modified electrodes in the air-saturated 10 mM pH 7.4 HEPES containing 0.3 M KCl solution. As shown, in addition to the reduction peak of dissolved oxygen near −0.5 V, no other redox peaks and no ECL signal were observed on GCE/TOAB (curve a). Similarly, the GCE/MOF-525/TOAB electrode (curve b) provides any ECL response, only the cathodic current became slightly larger compared to that of GCE/TOAB. This may be ascribed to the presence of MOF-525 that may generate a capactive effect. In contrast, a strong cathodic ECL signal occurred near −1.25 V and the ECL peak was located at −1.55 V for GCE/MOF-525-Zn/TOAB (Fig. 2B, curve c). Simultaneously, the other four strong reduction peaks were found at −0.89, −1.17, −1.34 and −1.58 V (from I to IV), and the more obvious oxidation peak was seen at −0.83 V on GCE/MOF-525-Zn/TOAB (Fig. 2A, curve c). This phenomenon is similar to our previous research,[21] the first reduction peak (Peak I, −0.89 V) should be attributed to the reduction of transition metal zinc in porphyrin ring ($Zn^{2+/\bullet+}$TCPP), and the two middle weak peaks (Peak II, −1.17 V and Peak III, −1.34 V) can be determined from the continuous electro-reduction of porphyrin ring ($Zn^{\bullet+}TCPP^{0/\bullet-}$ and $Zn^{\bullet+}TCPP^{\bullet-/2-}$); the last reduction peak (Peak I, −1.58 V) is assigned to $Zn^{\bullet+/0}TCPP^{2-}$. Thus, the generation of transient intermediate $Zn^{\bullet+}TCPP^{\bullet-}$ on the MOF-525-Zn frameworks preceded the electron-injection of Zn^{0}TCPP and the hydrogen evolution.

Furthermore, the effect of dissolved oxygen on the electrochemical and ECL behaviours of GCE/MOF-525-Zn/TOAB was investigated in Fig. 2C and D. Specifically, no ECL response of modified electrode was observed in the N_2-saturated environment (Fig. 2D, curve a). With the increase of dissolved oxygen concentration, the cathodic current gradually increased (Fig. 2C, curve a, b, c), highlighting the electrocatalytic role of

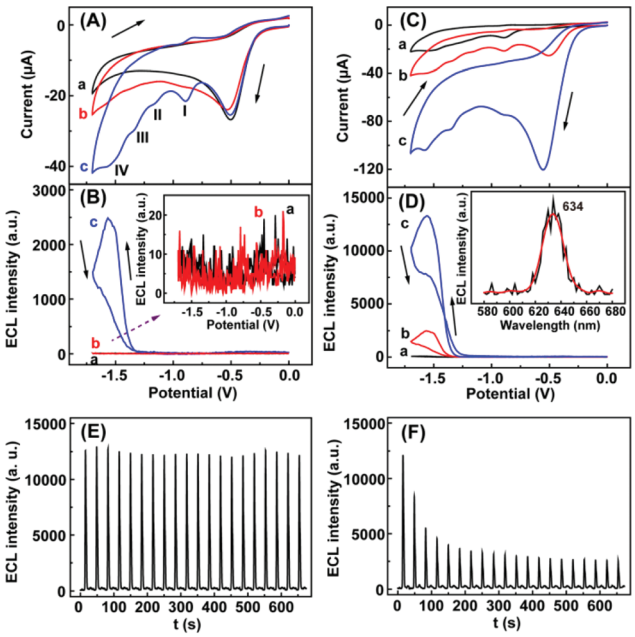

Fig. 2 (A) CVs and (B) ECL-potential curves of GCE/TOAB (a), GCE/MOF-525/TOAB (b), and GCE/MOF-525-Zn/TOAB (c) in the air-saturated pH 7.4 HEPES solution. Inset B: amplified curves a and b. (C) CVs and (D) ECL–potential curves of GCE/MOF-525-Zn/TOAB in the N_2-saturated (a), air-saturated (b), and O_2-saturated (c) pH 7.4 HEPES solution. Inset D: ECL spectrum of GCE/MOF-525-Zn/TOAB in the O_2-saturated pH 7.4 HEPES solution biased at −1.5 V. (E) ECL–time response of GCE/MOF-525-Zn/TOAB recorded in O_2-saturated pH 7.4 HEPES solution during a continuous potential scan between −1.7 and 0 V. Scan rate: 100 mV s^{-1}. (F) ECL–time response of GCE/MOF-525-Zn/TOAB recorded in the O_2-saturated pH 7.4 HEPES solution containing 10 mM NaN_3 during a continuous potential scan between −1.7 and 0 V. Scan rate: 100 mV s^{-1}.

porphyrin ring towards O_2 reduction.[56,57] Meanwhile, an ECL intensity peak up to 2489 a.u. was found under the air-saturated condition (Fig. 2D, curve b). Under the O_2-saturated condition (Fig. 2D, curve c), the ECL signal became stronger and the peak intensity increased to 13 314 a.u., which was about 5.35 times higher than that of the former, indicating that the ECL signal of GCE/MOF-525-Zn/TOAB greatly depends on the existence and concentration of dissolved oxygen.

Moreover, the ECL spectrum of GCE/MOF-525-Zn/TOAB in the O_2-saturated aqueous electrolyte solution biased at −1.5 V was performed in the inset of Fig. 2D. As shown, the ECL emission at 634 nm was observed, this result is consistent with our previous study,[21] owing to the $^1O_2$ dimol state involving collisions of two $^1O_2$ molecules.[17,58]

The ECL measurements of GCE/MOF-525-Zn/TOAB under the O_2-saturated condition upon continuous cyclic scans displayed constant and stable signals with relative standard deviation (RSD) of 1.4%, indicating the excellent reproducibility and stability of the ECL process attributed to the highly regular porous structure of MOFs for the enrichment of oxygen molecules (Fig. 2E). In addition, the ECL signal gradually weakened in the presence of 10 mM NaN_3 O_2-saturated solu-

tion because of $^1O_2$ quenching, caused by NaN_3 (Fig. 2F).[59] Based on the above experimental results and discussion, the possible ECL mechanism is proposed in Scheme 2B with the following equations:

$$O_2 + e^- \rightarrow O_2^{\bullet -} \quad (1)$$

$$\text{MOF-525}(Zn^{2+}\text{TCPP}) + e^- \rightarrow \text{MOF-525}(Zn^{\bullet +}\text{TCPP}) \quad (2)$$

$$\text{MOF-525}(Zn^{\bullet +}\text{TCPP}) + e^- \rightarrow \text{MOF-525}(Zn^{\bullet +}\text{TCPP}^{\bullet -}) \quad (3)$$

$$\text{MOF-525}(Zn^{\bullet +}\text{TCPP}^{\bullet -}) + O_2^{\bullet -} \rightarrow \text{MOF-525}(Zn^{\bullet +}\text{TCPP}^{2-}) + {}^1O_2 \quad (4)$$

$$2\,{}^1O_2 \rightarrow ({}^1O_2)_2^* \quad (5)$$

$$({}^1O_2)_2^* \rightarrow 2\,{}^3O_2 + h\nu \ (\lambda_{ex} = 634\,\text{nm}) \quad (6)$$

In addition, it should be noted here that the surfactant TOAB has a paramount influence on the ECL system. No ECL signal was found on GCE/MOF-525-Zn (Fig. 3A) in the air-saturated pH 7.4 HEPES solution. And the water contact angles (CAs) were measured to be 126° and 77° for MOF-525-Zn and MOF-525-Zn/TOAB on the clean glass plates, respectively (inset of Fig. 3A). The change in the value of CA reveals the hydrophobicity/hydrophilicity property of the surface. The relatively large CA for MOF-525-Zn can be ascribed to an abundance of hydrophobic porphyrin molecules on the frameworks. After the addition of TOAB, an amphipathic surfactant, the CA decreased dramatically due to hydrophilic groups, suggesting that TOAB encompassed porphyrin molecule orderly into an amphipathic membrane in aqueous media and the dissolved oxygen was allowed to infiltrate through it. Not only overcame the aggregation of ZnTCPP recognition sites but also facilitated dissolved oxygen to interact with recognition sites in virtue of the high surface and intrinsic open structure of MOFs.

Of course, the effect of TOAB concentration on GCE/MOF-525-Zn/TOAB cannot be neglected. As shown in Fig. 3B, the ECL intensity increased correspondingly in the range of 0–10 mM and gradually declined with further addition of TOAB. It indicates that a high concentration of TOAB could hinder electron transfer and chemical reactions between MOF-525-Zn and dissolved oxygen, and then the $^1O_2$ yield was reduced. To obtain high response, 10 mM TOAB was selected for the subsequent experiments.

In order to obtain the best ECL response, the ECL behaviours of GCE/MOF-525-Zn/TOAB were first tested in several commonly used aqueous media, including phosphate-buffered saline (PBS), Tris-HCl buffer, HEPES buffer, borate buffer and carbonate buffer. The strongest ECL intensity was obtained in the HEPES buffer (Fig. S2A†). Therefore, HEPES buffer is used as electrolyte solution. It is encouraging that the pH has no significant effect on the ECL response of GCE/MOF-525-Zn/TOAB (Fig. S2B†), indicating the ECL behaviours of MOF-525-Zn are fairly stable both in the acid and base environment.

Characterization and analytical performance of the biosensor

Characterization of the biosensor. EIS was applied to characterize the self-assembled process of the proposed biosensor using $Fe(CN)_6^{4-/3-}$ as a sensitive redox probe. The impedance data were fitted to an equivalent electronic circuit, shown as an inset in Fig. 4A, which includes the following four elements: the resistance of the electrolyte solution, R_s; the charge-transfer resistance, R_{ct}; the Warburg impedance, Z_w, resulting from diffusion of the redox probe; and the interface capacity, C_{dl}, modified by a constant phase element (CPE) to replace the classical capacitance accounting for the inhomogeneity of the electrode surface. As shown, after AuNPs were electrodeposited onto the surface of GCE, the charge-transfer resistance (R_{ct}) decreased significantly and only a straight line was observed in the whole frequency region (curve b), attributed to the excellent electrical conductivity of AuNPs. With the cysteine-kemptide assembled through the formation of Au–S bond (curve c), the value of R_{ct} increased significantly. After incubation with MCH (curve d) to saturate the thiol–gold interactions, the diameter of the semicircle increased again, indicating clearly that MCH blocks the diffusion of the redox probe and increased the interface electron transfer resistance. Afterwards, the R_{ct} value further increased after the phosphorylation reaction (curve e) owing to the electronic repulsion

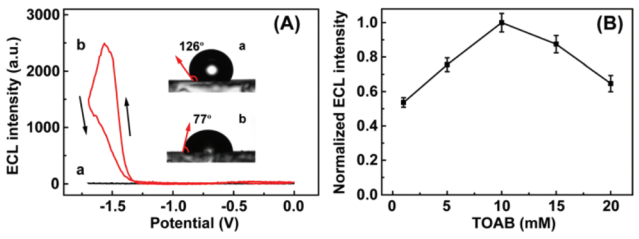

Fig. 3 (A) ECL–potential curves of GCE/MOF-525 (a) and GCE/MOF-525-Zn/TOAB (b) in the air-saturated pH 7.4 HEPES solution. Inset A: contact angle measurement images of MOF-525-Zn (a) and MOF-525-Zn/TOAB (b) on the glass plates. (B) Effect of TOAB concentration on the ECL peak intensity responses of GCE/MOF-525-Zn/TOAB in the O_2-saturated pH 7.4 HEPES solution. Error bars, SD, n = 3.

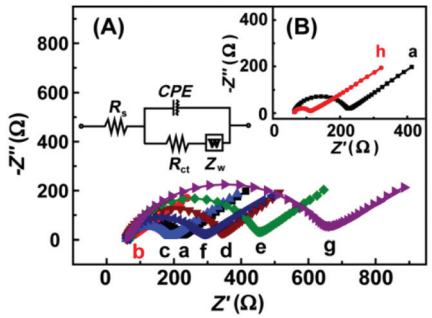

Fig. 4 (A) and (B) EIS for each immobilized step in 0.1 M KCl solution containing 5 mM $[Fe(CN)6]^{4-/3-}$: (a) bare GCE, (b) GCE/AuNPs, (c) GCE/AuNPs/kemptide, (d) GCE/AuNPs/kemptide/MCH, (e) GCE/AuNPs/phosphorylated kemptide/MCH, (f) GCE/AuNPs/phosphorylated kemptide/MCH/MOF-525-Zn, (g) GCE/AuNPs/phosphorylated kemptide/MCH/MOF-525-Zn/TOAB, and GCE/MOF-525-Zn (h). Inset A: equivalent circuit.

between the negatively charged phosphate groups and $Fe(CN)_6^{4-/3-}$. In contrast, the subsequent immobilization of MOF-525-Zn (curve f) *via* the formation of coordination bond between phosphate groups and Zr–O clusters on the MOF-525-Zn frameworks, induces a marked decrease of the R_{ct} value. Subsequently, the introduction of the surfactant TOAB caused a further increase on the R_{ct} value (curve g). Meanwhile, as shown in Fig. 4B, the R_{ct} value decreased significantly after modified MOF-525-Zn (curve h), demonstrating that MOF-525-Zn can significantly improve the electron transfer capacity of the modified electrode. It can be confirmed that the electron transfer resistance changed successively with sequential assembly of the biosensor for PKA assay.

Optimization of detection conditions. In order to achieve excellent ECL performance for the sensitive PKA assay, several experimental parameters including the concentration of kemptide and the concentration of ATP were optimized (Fig. 5). The effect of peptide concentration on catalytic reaction was estimated by incubating variety concentrations of peptides with 0.1 U mL^{-1} PKA and 80 μM ATP in the reaction buffer (Fig. 5A). The ECL intensity was enhanced with a peptide concentration up to 200 μM and then reached a pseudoplateau for higher concentrations of peptide. Therefore, the optimum peptide concentration was 200 μM. In addition, the other ATP substrate greatly influenced the PKA-catalyzed phosphorylation reaction. For increasing concentrations of ATP, ECL intensity initially showed a rapid increase in the range of 0 to 80 μM followed by a quasi-stabilization of ECL intensity (Fig. 5B). Consequently, 80 μM ATP was sufficient for the phosphorylation reaction catalyzed by PKA.

ECL detection of PKA. Fig. 6A showed the ECL responses of the proposed biosensor measured at various concentrations of PKA under the optimal experimental conditions. The ECL signal increases with the increasing concentrations of PKA and the resulting calibration curve is illustrated in Fig. 6B. The ECL peak intensity was proportional to the logarithm value of the PKA concentration in a range of 0.01 to 20 U mL^{-1}. The linear relationship can be represented as I (a.u.) = 1065.66 + 457.56 log C (U mL^{-1}) with a correlation coefficient of 0.997. The limit of detection (LOD) was estimated to be 0.005 U mL^{-1} (signal-to-noise ratio of 3), which was lower than that of previous reported studies.[60,61] The analytical methods and the key

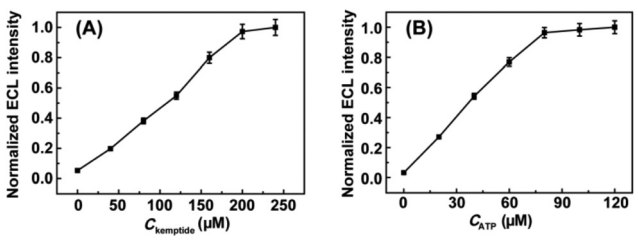

Fig. 5 Effects of (A) kemptide concentration and (B) ATP concentration on the ECL peak intensity responses of the biosensor. When one parameter changes, the others are under their optimal conditions. Error bars, SD, n = 3.

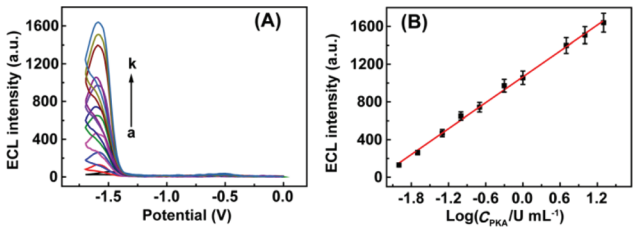

Fig. 6 (A) ECL–potential curves of the modified electrode at different concentrations of PKA (a–k: 0, 0.01, 0.02, 0.05, 0.1, 0.2, 0.5, 1.0, 5.0, 10.0, and 20.0 U mL^{-1}). (B) The calibration plots of ECL peak intensity *versus* the logarithm of PKA concentration. Error bars, SD, n = 3.

performance characteristics for PKA activity detection are compared and the results were summarized in Table S1.† The high sensitivity and wide linear range can be attributed to the high surface-to volume ratio with more photoelectric active sites on the MOF-525-Zn frameworks and larger surface area for dissolved oxygen molecules to react.

Stable ECL response was observed with relative standard deviations (RSD) of 0.53% when the biosensor was tested in the O_2-saturated pH 7.4 HEPES solution upon 10 cycles of continuous cyclic scans between 0 and −1.7 V (Fig. S3†), indicating the excellent ECL potential cycling stability for PKA assay. The reproducibility of the proposed ECL biosensor was also evaluated by measuring 0.1 U mL^{-1} of PKA activity ten times and the variation coefficient was 4.7%, which constitutes an acceptable reproducibility.

PKA detection in complex biological samples. To evaluate the as-designed sensors' general applicability in complex biological samples, the phosphorylation reaction solution was prepared by adding a desired amount of PKA in human serum instead of buffer solution. As shown in Table S2,† the recoveries were in the range of 93–105% for measurement of 0.1, 1.0 and 10.0 U mL^{-1} PKA, and the corresponding RSD were calculated to be 2.1%, 2.3% and 2.6%, suggesting that the proposed ECL biosensor could be applied for PKA detection with great accuracy and reliability.

Inhibition assay. The application and screening of kinase inhibitors for the regulation of kinase activity is important in disease diagnosis and clinical therapy. The ECL biosensor based on MOF-525-Zn was also used to quantitatively characterize the inhibition of kinase in the presence of small molecule inhibitors. In brief, the PKA-catalyzed phosphorylation reaction could be suppressed by the specific inhibitor of PKA, resulting in less phosphate group sites coordination binding Zr–O clusters of MOF-525-Zn, and then the ECL signal from the assembly modified electrode would weakened. As shown in Fig. 7, the ECL signal decreased correspondingly with increasing concentration of ellagic acid, cell-permeable antioxidant with antimutagenic and anticarcinogenic characteristics, and only weak ECL signal was observed with the addition of ellagic acid at 10 μM (curve a). From this, the half-maximal inhibition values (IC_{50}) for ellagic acid was calculated to be 3.57 μM, which is comparable with some previous results.[61,62] In

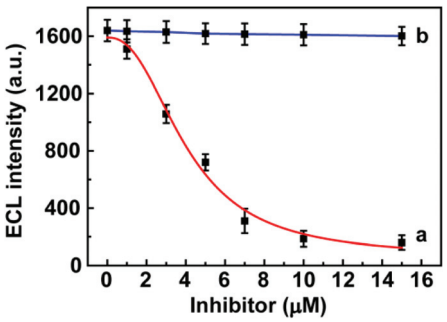

Fig. 7 Relationship between ECL peak intensity and concentrations of ellagic acid (a) and Tyrphostin AG 1478 (b). The concentrations of PKA and ATP are 20 U mL^{-1} and 80 μM, respectively. Error bars, SD, n = 3.

addition, Tyrphostin AG 1478, a tyrosine kinase inhibitor but not a PKA inhibitor, was also employed to evaluate the specificity of the proposed ECL biosensor. The ECL response had little change even though the concentration of Tyrphostin AG 1478 was as high as 15 μM (curve b), exhibiting excellent specificity for kinase inhibitor screening.

Conclusions

In summary, a novel Zr-based MOFs with zinc porphyrin inducing singlet oxygen ECL biosensor has been developed for protein kinase activity and inhibition assay. The as-synthesized MOF-525-Zn serves as a three-in-one platform possessing oxygen nanocage, electron media, and bonding site in the ECL bioanalysis system. Specifically, depending on the enrichment of oxygen molecules from the high porosity and tunable structures of MOFs, the active center ZnTCPP in MOF-525-Zn as electron media reacts with O_2 in the 3D nanocage to produce $^1O_2$, resulting in ECL signal. In addition, the amphiphilic surfactant TOAB facilitated O_2 to interact with electroactive ZnTCPP of MOF-525-Zn. Furthermore, with the coordination of the phosphate groups and inorganic Zr–O clusters as binding sites in MOF-525-Zn structures, MOF-525-Zn can be used as signal amplifying probes for an ultrasensitive ECL PKA assay. This three-in-one approach not only exhibits great promise in clinic diagnostics and targeted therapy, but also provides a novel promising platform for bioanalysis.

Acknowledgements

This research was supported by National Natural Science Foundation of China (Grant No. 21175114, 51572128), National Key Basic Research Program of China (2014CB931702), Qing Lan project of Jiangsu Province, the Fundamental Research Funds for the Central Universities (30915015101), and a project founded by the priority academic program development of Jiangsu Higher Education Institutions (PAPD).

Notes and references

1 G. L. Johnson and R. Lapadat, *Science*, 2002, **298**, 1911–1912.
2 H. Nie, S. Liu, R. Yu and J. Jiang, *Angew. Chem., Int. Ed.*, 2009, **48**, 9862–9866.
3 K. Newton, D. L. Dugger, K. E. Wickliffe, N. Kapoor, M. C. de Almagro, D. Vucic, L. Komuves, R. E. Ferrando, D. M. French and J. Webster, *Science*, 2014, **343**, 1357–1360.
4 M. A. Lemmon and J. Schlessinger, *Cell*, 2010, **141**, 1117–1134.
5 H. Cho, J. Mu, J. K. Kim, J. L. Thorvaldsen, Q. Chu, E. B. Crenshaw, K. H. Kaestner, M. S. Bartolomei, G. I. Shulman and M. J. Birnbaum, *Science*, 2001, **292**, 1728–1731.
6 P. Cohen, *Nat. Rev. Drug Discovery*, 2002, **1**, 309–315.
7 J. Zhou, X. Xu, W. Liu, X. Liu, Z. Nie, M. Qing, L. Nie and S. Yao, *Anal. Chem.*, 2013, **85**, 5746–5754.
8 J. Zhou, X. Xu, X. Liu, H. Li, Z. Nie, M. Qing, Y. Huang and S. Yao, *Biosens. Bioelectron.*, 2014, **53**, 295–300.
9 T. Li, D. Liu and Z. Wang, *Biosens. Bioelectron.*, 2009, **24**, 3335–3339.
10 Z. Deng, M. Ye, Y. Bian, Z. Liu, F. Liu, C. Wang, H. Qin and H. Zou, *Chem. Commun.*, 2014, **50**, 13960–13962.
11 J. J. Xu, W. W. Zhao, S. P. Song, C. H. Fan and H. Y. Chen, *Chem. Soc. Rev.*, 2014, **43**, 1601–1611.
12 R. P. Liang, C. Y. Xiang, H. F. Zhao and J. D. Qiu, *Anal. Chim. Acta*, 2014, **812**, 33–40.
13 H. F. Zhao, R. P. Liang, J. W. Wan and J. D. Qiu, *Chem. Commun.*, 2015, **51**, 12669–12672.
14 J. Liu, X. He, K. Wang, D. He, Y. Wang, Y. Mao, H. Shi and L. Wen, *Biosens. Bioelectron.*, 2015, **70**, 54–60.
15 S. Xu, Y. Liu, T. Wang and J. Li, *Anal. Chem.*, 2010, **82**, 9566–9572.
16 E. A. Mayeda and A. J. Bard, *J. Am. Chem. Soc.*, 1973, **95**, 6223–6226.
17 S. Senthil Kumar and A. J. Bard, *Anal. Chem.*, 2012, **85**, 292–295.
18 J. Schmitt, V. Heitz, A. Sour, F. Bolze, H. Ftouni, J. F. Nicoud, L. Flamigni and B. Ventura, *Angew. Chem., Int. Ed.*, 2015, **54**, 169–173.
19 S. Singh, A. Aggarwal, N. D. K. Bhupathiraju, G. Arianna, K. Tiwari and C. M. Drain, *Chem. Rev.*, 2015, **115**, 10261–10306.
20 K. M. Kadish, K. M. Smith and R. Guilard, *The Porphyrin Handbook: Bioinorganic and bioorganic chemistry*, Academic Press, Oxford, UK, 2003.
21 G. Y. Zhang, S. Y. Deng, X. J. Zhang and D. Shan, *Electrochim. Acta*, 2016, **190**, 64–68.
22 S. Y. Deng, T. T. Zhang, X. Ji, Y. Wan, P. Xin, D. Shan and X. J. Zhang, *Anal. Chem.*, 2015, **87**, 9155–9162.
23 R. F. Lobo, *Nature*, 2006, **443**, 757–758.
24 H. Furukawa, K. E. Cordova, M. O'Keeffe and O. M. Yaghi, *Science*, 2013, **341**, 1230444.
25 S. Furukawa, J. Reboul, S. Diring, K. Sumida and S. Kitagawa, *Chem. Soc. Rev.*, 2014, **43**, 5700–5734.

26 M. P. Suh, J. Park, T. K. Prasad and D. W. Lim, *Chem. Rev.*, 2011, **112**, 782–835.
27 P. Horcajada, R. Gref, T. Baati, P. K. Allan, G. Maurin, P. Couvreur, G. Férey, R. Morris and C. Serre, *Chem. Rev.*, 2011, **112**, 1232–1268.
28 A. Corma, H. Garcia and F. X. Llabrés i Xamena, *Chem. Rev.*, 2010, **110**, 4606–4655.
29 L. E. Kreno, K. Leong, O. K. Farha, M. Allendorf, R. P. Van Duyne and J. T. Hupp, *Chem. Rev.*, 2011, **112**, 1105–1125.
30 Z. Hu, B. J. Deibert and J. Li, *Chem. Soc. Rev.*, 2014, **43**, 5815–5840.
31 J. R. Li, J. Sculley and H. C. Zhou, *Chem. Rev.*, 2011, **112**, 869–932.
32 A. Morozan and F. Jaouen, *Energy Environ. Sci.*, 2012, **5**, 9269–9290.
33 Z. Peng, S. A. Freunberger, L. J. Hardwick, Y. Chen, V. Giordani, F. Bardé, P. Novák, D. Graham, J. M. Tarascon and P. G. Bruce, *Angew. Chem., Int. Ed.*, 2011, **50**, 6351–6355.
34 Y. C. Lu, H. A. Gasteiger and Y. Shao-Horn, *J. Am. Chem. Soc.*, 2011, **133**, 19048–19051.
35 M. Jahhan, Q. Bao and K. P. Loh, *J. Am. Chem. Soc.*, 2012, **134**, 6707–6713.
36 W. Zhang, Z. Y. Wu, H. L. Jiang and S. H. Yu, *J. Am. Chem. Soc.*, 2014, **136**, 14385–14388.
37 S. Shimomura, M. Takata and S. Kitagawa, *Nat. Chem.*, 2010, **2**, 633–637.
38 M. Jiang, L. Li, D. Zhu, H. Zhang and X. Zhao, *J. Mater. Chem. A*, 2014, **2**, 5323–5329.
39 W. Y. Gao, M. Chrzanowski and S. Ma, *Chem. Soc. Rev.*, 2014, **43**, 5841–5866.
40 W. F. Ma, C. Zhang, Y. T. Zhang, M. Yu, J. Guo, Y. Zhang, H. J. Lu and C. C. Wang, *Langmuir*, 2014, **30**, 6602–6611.
41 M. Zhao, C. Deng and X. Zhang, *Chem. Commun.*, 2014, **50**, 6228–6231.
42 X. Zhu, B. Li, J. Yang, Y. Li, W. Zhao, J. Shi and J. Gu, *ACS Appl. Mater. Interfaces*, 2014, **7**, 223–231.
43 G. Y. Zhang, S. Y. Deng, W. R. Cai, S. Cosnier, X. J. Zhang and D. Shan, *Anal. Chem.*, 2015, **87**, 9093–9100.
44 G. Della Giustina, A. Zambon, F. Lamberti, N. Elvassore and G. Brusatin, *ACS Appl. Mater. Interfaces*, 2015, **7**, 13280–13288.
45 H. L. Jiang, D. Feng, K. Wang, Z. Y. Gu, Z. Wei, Y. P. Chen and H. C. Zhou, *J. Am. Chem. Soc.*, 2013, **135**, 13934–13938.
46 N. C. Burtch, H. Jasuja and K. S. Walton, *Chem. Rev.*, 2014, **114**, 10575–10612.
47 J. E. Mondloch, M. J. Katz, N. Planas, D. Semrouni, L. Gagliardi, J. T. Hupp and O. K. Farha, *Chem. Commun.*, 2014, **50**, 8944–8946.
48 C. W. Kung, T. H. Chang, L. Y. Chou, J. T. Hupp, O. K. Farha and K. C. Ho, *Chem. Commun.*, 2015, **51**, 2414–2417.
49 T. H. Chang, C. W. Kung, H. W. Chen, T. Y. Huang, S. Y. Kao, H. C. Lu, M. H. Lee, K. M. Boopathi, C. W. Chu and K. C. Ho, *Adv. Mater.*, 2015, **27**, 7229.
50 W. Morris, B. Volosskiy, S. Demir, F. Gándara, P. L. McGrier, H. Furukawa, D. Cascio, J. F. Stoddart and O. M. Yaghi, *Inorg. Chem.*, 2012, **51**, 6443–6445.
51 S. Afzal, W. A. Daoud and S. J. Langford, *J. Mater. Chem.*, 2012, **22**, 4083–4088.
52 J. Rochford, D. Chu, A. Hagfeldt and E. Galoppini, *J. Am. Chem. Soc.*, 2007, **129**, 4655–4665.
53 K. M. Kadish, K. M. Smith and R. Guilard, *The Porphyrin Handbook: Electron Transfer*, Academic Press, San Diego, USA, 2000.
54 G. Parkin, *Chem. Rev.*, 2004, **104**, 699–767.
55 J. S. Anderson, A. Gallagher, J. A. Mason and T. D. Harris, *J. Am. Chem. Soc.*, 2014, **136**, 16489–16492.
56 A. J. Bard and L. R. Faulkner, *Electrochemical Methods: Fundamentals and Applications*, Wiley, New York, USA, 1980.
57 S. Samanta, K. Mittra, K. Sengupta and S. Chatterjee, *Inorg. Chem.*, 2013, **52**, 1443–1453.
58 A. U. Khan and M. Kasha, *J. Am. Chem. Soc.*, 1970, **92**, 3293–3300.
59 H. Wang, X. Yang, W. Shao, S. Chen, J. Xie, X. Zhang, J. Wang and Y. Xie, *J. Am. Chem. Soc.*, 2015, **137**, 11376–11382.
60 X. Xu, J. Zhou, X. Liu, Z. Nie, M. Qing, M. Guo and S. Yao, *Anal. Chem.*, 2012, **84**, 4746–4753.
61 Z. Wang, N. Sun, Y. He, Y. Liu and J. Li, *Anal. Chem.*, 2014, **86**, 6153–6159.
62 Z. Yan, Z. Wang, Z. Miao and Y. Liu, *Anal. Chem.*, 2016, **88**, 922–929.